JGR Space Physics

RESEARCH ARTICLE
10.1029/2025JA033977

Unraveling the Velocity Evolution of High-Speed Jets in Earth's Magnetosheath

Yuxiang Wang[1,2], Xinliang Gao[1,2], Jiuqi Ma[1,2], Quanming Lu[1,2], San Lu[1,2], and Junyi Ren[1,2]

[1]CAS Key Lab of Geospace Environment, School of Earth and Space Sciences, University of Science and Technology of China, Hefei, China, [2]CAS Center for Excellence in Comparative Planetology, Hefei, China

Key Points:

- We compiled a comprehensive data set of high-speed jets (HSJs) from MMS, THEMIS, and Cluster, with the occurrence rate peaking in the middle magnetosheath
- During HSJ penetration, anti-sunward speed keeps declining, while $|V_{y,z}|$ increases near the magnetopause due to magnetopause deflection
- HSJ transverse velocity tends to align with magnetosheath flow early on, showing overall isotropy and a slight duskward preference

Supporting Information:

Supporting Information may be found in the online version of this article.

Correspondence to:

X. Gao,
gaoxl@mail.ustc.edu.cn

Citation:

Wang, Y., Gao, X., Ma, J., Lu, Q., Lu, S., & Ren, J. (2026). Unraveling the velocity evolution of high-speed jets in Earth's magnetosheath. *Journal of Geophysical Research: Space Physics*, *131*, e2025JA033977. https://doi.org/10.1029/2025JA033977

Received 17 MAR 2025
Accepted 12 JAN 2026

Abstract High-speed jets (HSJs) are transient phenomena characterized by significant enhancement of magnetosheath dynamic pressure. They are capable of traversing the magnetosheath and impinging upon the magnetopause, triggering a diverse array of geoeffects. However, the evolution of HSJs during their propagation from the bow shock to the magnetopause still remains unclear. Leveraging multi-satellite data from MMS (2015–2023), THEMIS (2008–2023), and Cluster (2001–2020), we have compiled a comprehensive data set of nearly 40,000 HSJs to statistically study the velocity evolution of HSJs from the bow shock to the magnetopause for the first time. It is shown that the occurrence rate of HSJs depends on their relative positions within the magnetosheath, peaking in the middle region. Typically, in the GSE coordinates, as HSJs penetrate into the magnetosheath, the V_x component gradually decreases until they reach the magnetopause, where HSJs are deflected and their V_y and V_z components are enhanced. Meanwhile, some HSJs are redirected backwards owing to rebounce of the magnetopause, resulting in the sunward flow. Notably, the velocity-direction distribution of HSJs in the (y,z)-plane is largely isotropic overall yet exhibits a subtle dusk-favored asymmetry. This distribution aligns with the background flow throughout the evolution of HSJs, a feature that is consistent with the outcomes of 3-D global simulations. This strong consistency implies HSJ transverse velocity tends to align with the ambient magnetosheath flow even early in their evolution. Our study provides some new insights in better understanding the evolution of HSJs within the magnetosheaths of Earth and other planets.

1. Introduction

High-speed jets (HSJs) are regarded as remarkable enhancements of the dynamic pressure in the Earth's magnetosheath, widely pervasive downstream of the quasi-parallel bow shock (Hietala et al., 2009; Hietala & Plaschke, 2013; Nemecek et al., 1998; Plaschke et al., 2018). HSJs are typically observed to be associated with a concurrent increase in both velocity and density (M. O. Archer & Horbury, 2013; Preisser et al., 2020), while their magnetic fields can either exhibit an increase or a decrease (Plaschke et al., 2013; M. O. Archer & Horbury, 2013). Various formation mechanisms for magnetosheath jets have been proposed, encompassing the interaction of compressive structures with the quasi-parallel bow shock (Karlsson et al., 2015; Ren et al., 2023; Suni et al., 2021), shock reformation (Raptis, Karlsson, Vaivads, Pollock, et al., 2022), and other processes (Guo et al., 2022; Y. Zhou et al., 2023; Fatemi et al., 2024; Osmane & Raptis, 2024). They are attracting more and more attention as they can exert a significant impact on the magnetopause, thereby resulting in diverse geoeffects (Krämer et al., 2025). For instance, the impact of HSJs can cause a local indentation of magnetopause (J. H. Shue et al., 2009), possibly triggering local magnetic reconnection (Hietala et al., 2018; Karimabadi et al., 2014), generating magnetopause boundary surface waves (M. Archer et al., 2019), and causing localized auroral brightening (Han et al., 2017; B. Wang et al., 2018; Z. Wang et al., 2025). Besides, HSJs are capable of modulating plasma waves in the magnetosphere, leading to the prompt disappearance of chorus waves (X. Zhou et al., 2024). Overall, the response of the magnetopause to the strike of HSJ can be roughly described as the "Indentation-Rebounce-Relaxation" sequence, during which a pair of field-aligned currents may emerge as a consequence of the compression or rebounce of magnetopause (Ma et al., 2024).

However, HSJs need to penetrate and traverse the relatively slow-moving magnetosheath plasma in order to reach the magnetopause boundary layer (Krämer et al., 2025). Therefore, it is fundamentally important to understand how the HSJs propagate and evolve in the magnetosheath from the bow shock to the magnetopause. Plaschke et al. (2017) presented some evidence that the HSJs can compress and push aside the slower ambient magnetosheath plasma at the leading edge, thereby stirring the magnetosheath. Moreover, both simulations and

observations have revealed that some supermagnetosonic HSJs drive bow waves at the leading edge due to the deflection and deceleration by the magnetic structure (Liu et al., 2020; Raptis, Karlsson, Vaivads, Lindberg, et al., 2022; Ren, Lu, et al., 2024; Vuorinen et al., 2022). Additionally, Dmitriev and Suvorova (2015) provided several examples where HSJs either penetrated the magnetopause, accompanied by a velocity decrease, or did not penetrate it, instead showing deflection. Nevertheless, it is challenging to establish the evolution pattern of HSJs solely based on case studies.

Statistical analysis is an alternative approach for investigating the evolution of magnetosheath jets, yet it is vitally dependent on the availability of a comprehensive database. Based on THEMIS data, Plaschke et al. (2013) have collected 2,859 HSJ events in the subsolar magnetosheath region from 2008 to 2011, and pointed out that the HSJs are more common near the bow shock. Later, with the MMS data, Raptis et al. (2020) assembled a data set consisting of 8,499 HSJ events in the subsolar magnetosheath from 2015 to 2019, and found that the HSJs are preferentially detected near the magnetopause. Recently, Poeppelwerth et al. (2024) also constructed a data set of HSJs from the Cluster data in the subsolar magnetosheath, but showed that the occurrence rate of HSJs peaks in the middle of the magnetosheath. It should be noted that these occurrences of HSJs are highly dependent on the criterion (Plaschke et al., 2018). For example, the criterion of M. O. Archer and Horbury (2013) may include flux transfer events near the magnetopause. Therefore, it is evident that the statistical results differ across various data sets, which is essentially caused by the different spatial and temporal extents covered by different missions.

Integrating data sets from multiple missions can be conducive to reducing statistical bias. In this study, we have constructed an extensive data set by integrating multi-satellite data from MMS (2015–2023), THEMIS (2008–2023), and Cluster (2001–2020) in the magnetosheath, which encompasses nearly 40,000 HSJs. Using this new data set, we have performed a statistical analysis of the velocity evolution of HSJs in the magnetosheath, and further preliminarily constructed their evolution pattern during their propagation in the magnetosheath. The data and method are briefly outlined in Section 2. Section 3 presents the statistics results, while Section 4 summarizes the conclusions and discussion.

2. Data and Methods

To get sufficiently good coverage of Earth's magnetosheath, we have combined the data from MMS, THEMIS, and Cluster to conduct this statistical analysis of HSJs. MMS mission, consisting of four identical spacecraft (denoted as MMS1 to MMS4), was launched on 12 March 2015, with an initial apogee of $12R_E$ (R_E is Earth radius) (Burch et al., 2016). The onboard Fluxgate Magnetometer (FGM) measures the magnetic field in survey mode (Russell et al., 2016). The proton moment data, such as density, velocity, temperature, and energy spectrum, are provided by the Fast Plasma Instrument (Pollock et al., 2016) with a time resolution of 4.5 s. Given the close spacing of the four MMS spacecraft, we only utilized MMS2 data when selecting HSJs to avoid double counting. Here the MMS data from September 2015 to June 2023 are utilized.

Similarly, THEMIS mission, comprising five identical spacecraft (denoted as THA to THE), was launched on 17 February 2007, and placed into a highly elliptical orbit with a geocentric apogee of 14.7 R_E (Angelopoulos, 2008). The velocity, density, temperature and the omnidirectional energy flux density of ions are obtained from the Electrostatic Analyzer (McFadden et al., 2008) with a time resolution of 3 s, while magnetic field measurements are conducted with the onboard FGM (Auster et al., 2008). The spatial separation of the THEMIS probes allows them to observe distinct HSJs. Hence, we utilized THEMIS data from all five probes, covering the period from January 2008 to September 2023.

Cluster mission, consisting of four identical spacecraft (denoted as C1 to C4), was launched in the summer of 2000 and placed into highly elliptical and polar orbits of 4 × 19.6 Earth R_E (Escoubet et al., 2001). Ion measurements like ion velocity, ion density, ion temperature and the ion omnidirectional energy flux density are obtained from the Hot Ion Analyzer of the Cluster Ion Spectrometry experiment (CIS-HIA) (Rème et al., 2001) with a time resolution of 4 s, and magnetic field measurements are provided by the FGM (Balogh et al., 1997). Since CIS-HIA was only operational on spacecraft C1 and C3 (Dandouras et al., 2010) and the CIS-HIA onboard C3 had been non-operational since 11 November 2009, we focused on data from C1 for this study, spanning January 2001 to December 2020.

Figure 1 presents the spatial coverage of the three missions, as well as the combined data set. In each panel, the coded color represents the normalized time for each spacecraft at every specific location. This normalized time is

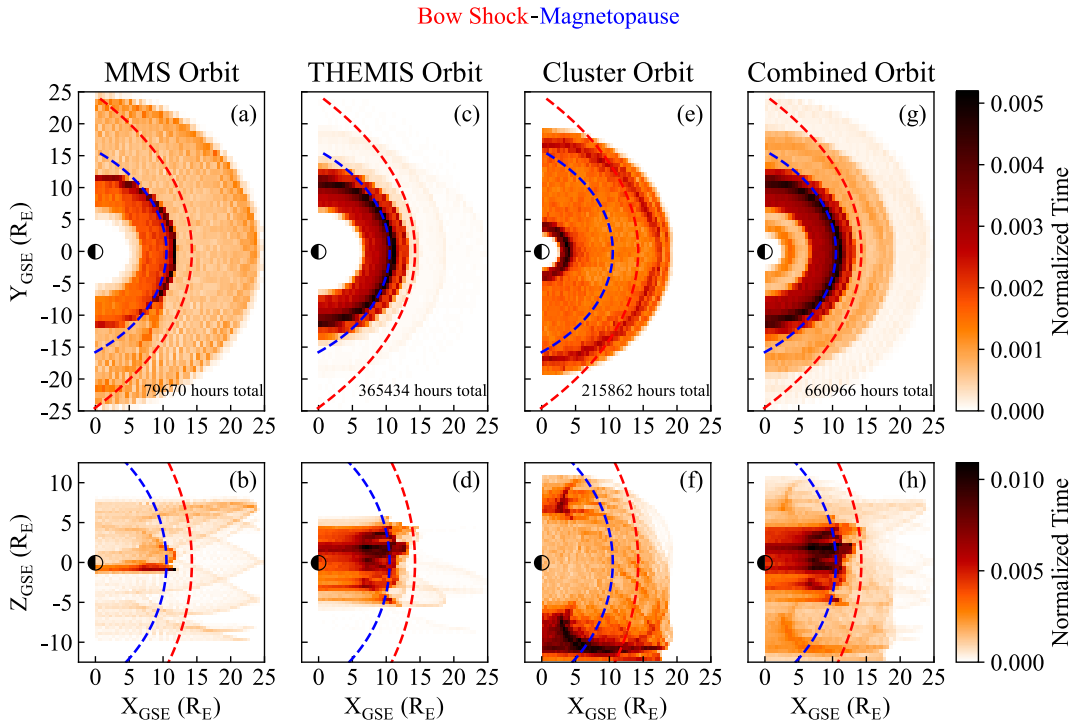

Figure 1. The orbital ($7\ R_E \leq r \leq 25\ R_E$) coverage for MMS (2015–2023), THEMIS (2008–2023), Cluster (2001–2020) and Combined Satellites in GSE coordinates. (a) MMS orbital coverage in the *xy*-plane, (b) MMS orbital coverage in the *xz*-plane, (c) THEMIS orbital coverage in the *xy*-plane, (d) THEMIS orbital coverage in the *xz*-plane, (e) Cluster orbital coverage in the *xy*-plane, (f) Cluster orbital coverage in the *xz*-plane, (g) Combined orbital coverage in the *xy*-plane, (h) Combined orbital coverage in the *xz*-plane. The red and blue dashed lines indicate the estimated positions of the bow shock model introduced by Chao et al. (2002) and the magnetopause model proposed by J. Shue et al. (1998), respectively, under the average solar wind conditions during 2001–2023. The spatial resolution of the bins in the *xy*-plane (first-row) panel is $0.55R_E \times 1.00R_E$, while that in the *xz*-plane (second-row) panel is $0.55R_E \times 0.50R_E$.

defined as the dwell time at a specific location divided by the respective total dwell time of MMS, THEMIS, Cluster, and the Combined Mission. The total dwell times are listed in the top panels, which corresponds to the cumulative duration during which the spacecrafts are located within the radial range of $7R_E < r < 25R_E$ region (r represents the radial distance from the Earth). For reference, we have also plotted the positions of the bow shock and magnetopause, which are estimated by the models proposed by Chao et al. (2002) and J. Shue et al. (1998) based on the average solar wind parameters during 2001–2023. As illustrated in Figures 1a and 1b, although the MMS spacecraft are able to generally traverse the dayside magnetosheath, the majority of their observational data is obtained in the vicinity of the magnetopause and around the magnetic equator. This is due to the spacecraft rapidly traversing the magnetosheath in the Phase 2 of MMS, with an apogee of around 25 R_E; by contrast, they lingered near the magnetopause (Phase 1) for extended periods when apogee was about 12 R_E. THEMIS spacecraft exhibit the longest dwell time, since we include all five probes in the database. Moreover, their spatial coverage bears a remarkable resemblance to that of MMS spacecraft (Figures 1c and 1d). Cluster spacecraft exhibit the different coverage from others, which can provide more observations in the vicinity of the bow shock and higher latitudes (i.e., larger Z_{GSE}, Figures 1e and 1f). Therefore, we combine the data from all three missions for studying the evolution of HSJs from bow shock to magnetopause, since the combined data set gives a better coverage as shown in Figures 1g and 1h.

The upstream solar wind conditions can be obtained from the OMNI website (https://omniweb.gsfc.nasa.gov) with the 1-min resolution, which have been time-shifted to Earth's bow shock nose. In this study, we have further adopted a 5-min average window for solar wind data and shifted it 5 min prior to each HSJ to establish a connection between HSJs and corresponding upstream solar wind conditions, similar to the procedure in Plaschke et al. (2013).

Before selecting HSJs, we first extract all the magnetosheath intervals from the database based on the method proposed by Song et al. (2021). Magnetosheath is identified via an enhanced algorithm using criteria on radial

distance, energy flux, and magnetic field variations. For more detailed information about this method, please refer to the Supporting Information S1. Although there exist many criteria of identifying HSJs in the literature, we have developed a new criterion based on the local magnetosheath dynamic pressure to fit the new database better. This criterion is obtained by slightly modifying the criterion used in M. O. Archer et al. (2012) and Koller et al. (2022), which is described as follows:

$$P_{\mathrm{dyn,msh}} \geq 2.0\langle P_{\mathrm{dyn,msh}}\rangle_{20\mathrm{min}} \tag{1}$$

$$P_{\mathrm{dyn,msh,max}} \geq 2.5\langle P_{\mathrm{dyn,msh}}\rangle_{20\mathrm{min}} \tag{2}$$

Where,

$$P_{\mathrm{dyn,msh}} = m_p n_i V_i^2 \tag{3}$$

and angular brackets denote the 20-min time averaging procedure. Additionally, we further required that the magnetic field component B_z (and other components) should not show significant reversals. Finally, we also visually inspected the data to exclude HSJs associated with FTEs or other events.

To test inter-calibration biases across MMS, THEMIS, and Cluster, we have compared key plasma parameters (ion velocity 3 components and number density) of HSJs in the mid-magnetosheath ($0.5 < F < 0.6$, peak occurrence; not shown), and consistent parameter distributions across missions confirm the inter-calibration uncertainties is negligible.

To enhance the comparability and rationality of our results, we further compare them with the global simulation conducted by Ren, Guo, et al. (2024). This simulation is performed at a realistic magnetospheric scale. For the solar wind parameters adopted herein: the ion number density is set to $N_i = 3.2\mathrm{cm}^3$, the IMF is $B = (3.72, 0.13, 0.21)\mathrm{nT}$, and the velocity is $V = (466.48, 12.86, 14.31)$ km/s. So, the Alfvén Mach number is $M_A = 12.27$ (Ren, Guo, et al., 2024).

3. Results

Figure 2 presents three time intervals extracted from MMS2, THC, and C1 observations, including the time series of ion dynamic pressure P_{dyn}, ion density n_i, magnetic field B_{GSE}, ion bulk velocity v_i, ion energy flux, and ion temperature T_i from top to bottom. In the top panels, the blue and green lines mark the 2.0-fold and 2.5-fold mean dynamic pressure over 20 min in the magnetosheath, respectively. These satellites were operating in the magnetosheath according to the ion energy flux (penultimate row). Based on the criteria specified above, we identify several HSJ intervals within these time periods, which are shaded in red. It should be noted that even though there might be more than one peak in dynamic pressure within the shaded region, we still document it as a single HSJ event. These selected HSJs exhibit several common properties consistent with previous observations (Nemecek et al., 1998; M. O. Archer et al., 2012; A. V. Dmitriev & Suvorova, 2012; Plaschke et al., 2013; M. O. Archer & Horbury, 2013), such as a relatively large bulk velocity and a low temperature.

In our data set, we have selected 38,494 HSJ events in total, including 4253 events from MMS, 32,197 from THEMIS, and 2044 from Cluster. Figure 3 illustrates the spatial distribution of HSJ counts in our data set, alongside the average positions of the bow shock and magnetopause. Specifically, Figures 3a and 3b display the observation counts in the GSE *xy*-plane and *xz*-plane. Notably, high-latitude HSJ events are extremely sparse due to constrained orbit inclination. When the HSJ observations are normalized with the dwell time, the HSJs are much more evenly distributed (Figures 3c and 3d). Overall, this HSJ data set can provide sufficient samples spanning from the bow shock to the magnetopause to conduct the statistical analysis of HSJs. It is worth noting that the data gap near the bow shock or the unexpected data inside the magnetopause is caused by the deviation between their average positions and instantaneous positions. Additionally, due to the projection of the 3D spatial distribution of HSJs onto 2D GSE coordinates, HSJs situated near the magnetopause in the non-subsolar magnetosheath appear to cluster more densely around the magnetopause than they actually do in 3D space.

To present the spatial evolution of HSJs, it is necessary to first define the location of each HSJ. Notably, a typical HSJ transits from the bow shock to the magnetopause in around 2 min, during which solar wind conditions can be

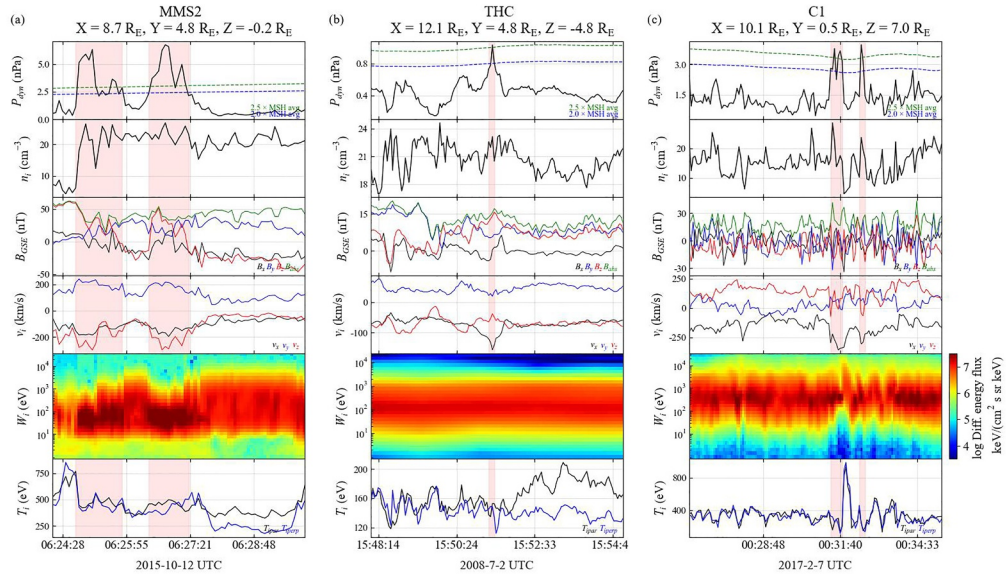

Figure 2. Examples of the magnetosheath jet observations from distinct satellite missions in the GSE coordinates. (a) MMS2, (b) THC, (c) C1. From top to bottom, in each subplot: dynamic pressure with 20-min averaged background values, ion number density, magnetic field, ion velocity, ion energy spectrum, and ion temperature. Red regions signify magnetosheath jet observations.

assumed unchanged. However, different solar wind conditions induce distinct magnetosheath structures. To address this, we used fractional distance (F) (M. O. Archer & Horbury, 2013) to normalize HSJ relative positions, ensuring consistent positional referencing across varying magnetosheath configurations. For each HSJ, we obtained the positions of the bow shock and magnetopause from Chao's and Shue's models based on the mean solar wind parameters during the HSJ's period. Then, we calculated the relative position F of the HSJ as below (M. O. Archer & Horbury, 2013):

$$F(r,|\theta|) = \frac{r - r_{\mathrm{mp}}(|\theta|)}{r_{\mathrm{bs}}(|\theta|) - r_{\mathrm{mp}}(|\theta|)}$$

Where, θ is the aberrated solar zenith angle, r is the radial distance of the HSJ, and r_{bs} and r_{mp} are the radial distances of the modeled bow shock and magnetopause, respectively. Therefore, $F = 0$ ($F = 1$) means that the HSJ is at the magnetopause (the bow shock). Because the estimated positions of the bow shock and magnetopause are subject to error, the F value for some HSJs may be negative or exceed unity. In such cases, we artificially set the F to zero or one to preclude any confusion.

The distribution of HSJs as a function of F is shown in Figure 4, where the occurrence rate of HSJs is calculated as the ratio of jet number to the time of magnetosheath observations at each F bin. To facilitate comparison with previous statistical studies, we have considered the HSJs both in the global region (Figure 4a) and in the subsolar region (Figure 4b). The global region encompasses the magnetosheath intervals with $X_{\mathrm{GSE}} > 0$, while the subsolar region is defined as the intervals when the spacecraft lies within a 30°-wide, Sun-centered conical volume with its apex at Earth (Plaschke et al., 2013). By employing the aforementioned algorithm, we obtained 30,977 hr of global magnetosheath data and 9,044 hr of subsolar magnetosheath data. In each panel, the black line denotes the combined occurrence rate, while the red, blue and orange dotted lines denote the occurrence rate based on the data from MMS, THEMIS and Cluster, respectively. The average occurrence rates are also listed in the upper-right corner. As shown in Figure 4a, the spatial distribution of HSJs for each mission exhibit substantial differences, which are attributed to the distinct orbital coverages of these missions across the global region. Specifically, THEMIS mainly detects HSJs in the low-latitude, magnetopause-side magnetosheath (similar to MMS Phase 1), while MMS Phase 2 also observes HSJs in the high-latitude, bow shock-side magnetosheath. Cluster complements with extensive high-latitude, bow shock-side HSJ data. Their combined data set maximizes spatial coverage, expands the

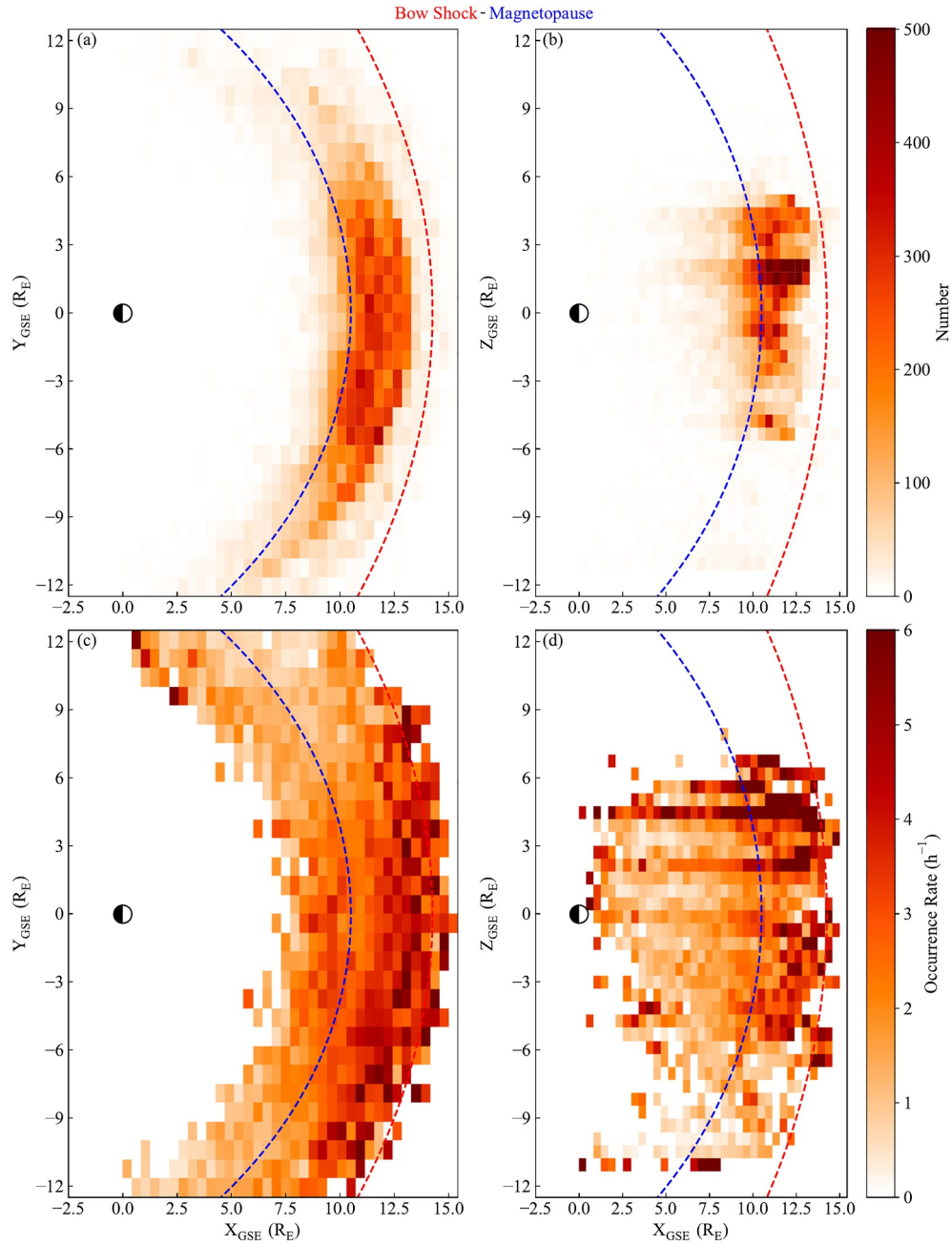

Figure 3. Spatial distribution of high-speed jets (HSJs) projected onto the *xy*-plane and *yz*-plane in GSE coordinates. (a) HSJs location distribution in *xy*-plane, (b) HSJs location distribution in *xz*-plane, (c) HSJs occurrence rate distribution in *xy*-plane, (d) HSJs occurrence rate distribution in *xz*-plane. The red and blue dashed lines indicate the estimated positions of the bow shock model introduced by Chao et al. (2002) and the magnetopause model proposed by J. Shue et al. (1998), respectively, under the average solar wind conditions of the HSJs data set.

event catalog and enabled more uniformly sampled solar wind conditions, supporting robust statistical analyses. The combined data set reveals that HSJs are frequently observed in the middle region of magnetosheath (F = 0.5–0.7; Figure 4a). The same preference can be easily found for the HSJs in the subsolar region regardless of which data set (Figure 4b), supporting previous studies (Plaschke et al., 2013; Poeppelwerth et al., 2024). The global and subsolar occurrence rates both peak in the mid-magnetosheath. This could be explained by the combined effect of HSJ deceleration-driven accumulation and dissipative processes. Other jet formation mechanisms that take place deeper in the magnetosheath, like firehose instability (Osmane &

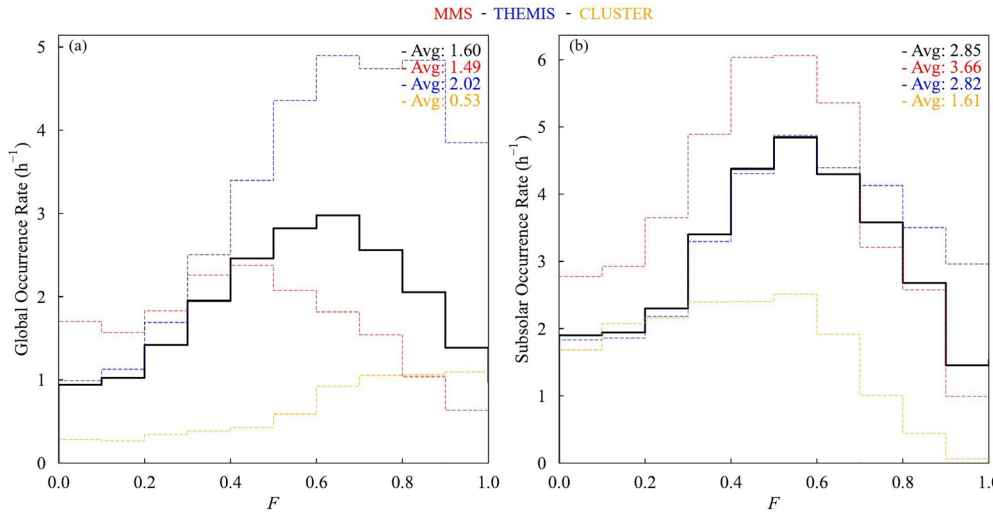

Figure 4. The occurrence rate of high-speed jets data set. (a) The occurrence rate histogram in the global magnetosheath, (b) The occurrence rate histogram in the subsolar magnetosheath. The red, blue, and yellow dotted lines denote the occurrence histogram from MMS, THEMIS, and Cluster respectively. The solid black line shows the occurrence histogram of the combined data set. The average occurrence rates calculated by MMS, THEMIS, Cluster, and the combined data set are listed in red, blue, orange and black fonts.

Raptis, 2024), may also exist. Based on the combined data set, the average occurrence rate of HSJs in the subsolar region is 2.85 per hr, which is roughly consistent with previous results from Plaschke et al. (2013) and Koller et al. (2022). The normalized occurrence rates of HSJs all peak in the mid-magnetosheath in the subsolar region, but for some missions, they peak near the bow shock when the full data set is included. This likely stems from non-subsolar HSJs having limited magnetosheath penetration (dissipating and failing to meet jet criteria near the magnetopause). This may be due to different shock geometries, as it has been shown that quasi-parallel shock-associated jets propagate deeper into the magnetosheath (Goncharov et al., 2020; LaMoury et al., 2021).

The HSJ occurrence rates vary across different missions (Figure 4), which stems from differences in solar wind conditions during each mission's operational period (Vuorinen, LaMoury et al., 2023). Figures 5a–5g illustrate the mean solar wind conditions for the global HSJ data sets of MMS, THEMIS, and Cluster, with key observations as follows: THEMIS-identified global HSJs are concentrated near the bow shock (Figure 4a). This is because, among the three data sets, THEMIS has the highest solar wind beta, highest solar wind Alfvén Mach number, highest dynamic pressure, and lowest IMF $|B|$ in the jet formation region ($F > 0.75$) (Vuorinen, Hietala, et al., 2023), which also explains its highest HSJ occurrence rate; In contrast, the global HSJ data set from MMS, characterized by the smallest IMF cone angle and highest solar wind speed, extends deeper into the magnetosheath. Specifically, it exhibits higher occurrence rates in the vicinity of the magnetopause (Figure 4a); Global Cluster HSJs, in the $F > 0.75$ region, have the lowest solar wind Beta and Alfvén Mach number, plus the highest IMF $|B|$ and cone angle, leading to their lowest occurrence rate (Figure 4a). Figures 5h–5n illustrate the differences in the mean solar wind conditions among the subsolar HSJs data sets from MMS, THEMIS, and Cluster. Notably, the discrepancies in solar wind conditions between MMS and THEMIS are significantly reduced, which results in a similar distribution of HSJs shown in Figure 4b; In contrast, the HSJ occurrence rate derived from Cluster remains the lowest, attributable to the lowest solar wind dynamic pressure, Alfvén Mach number, and beta (Figure 4b). Since solar wind conditions exhibit biases across distinct missions within each fractional distance (F) bin, we combine all available data sets to mitigate such bias in solar wind conditions for each F bin to a certain extent.

Figure 6 illustrates the evolution of HSJs from the bow shock to magnetopause, where the red solid line denotes the HSJs in the global region and the blue solid line denotes those in the subsolar region. In each F bin, the median value will be calculated, and the first and third quartiles will be utilized as the error bars. The median background magnetosheath flow (dotted line) is also plotted for reference. Just as expected, the x component of velocity (V_x) of HSJs gradually decreases as the HSJs travel from the bow shock toward the magnetopause, which is similar to the evolution of the background magnetosheath flow (Figure 6a). Notably, once the HSJs approach the

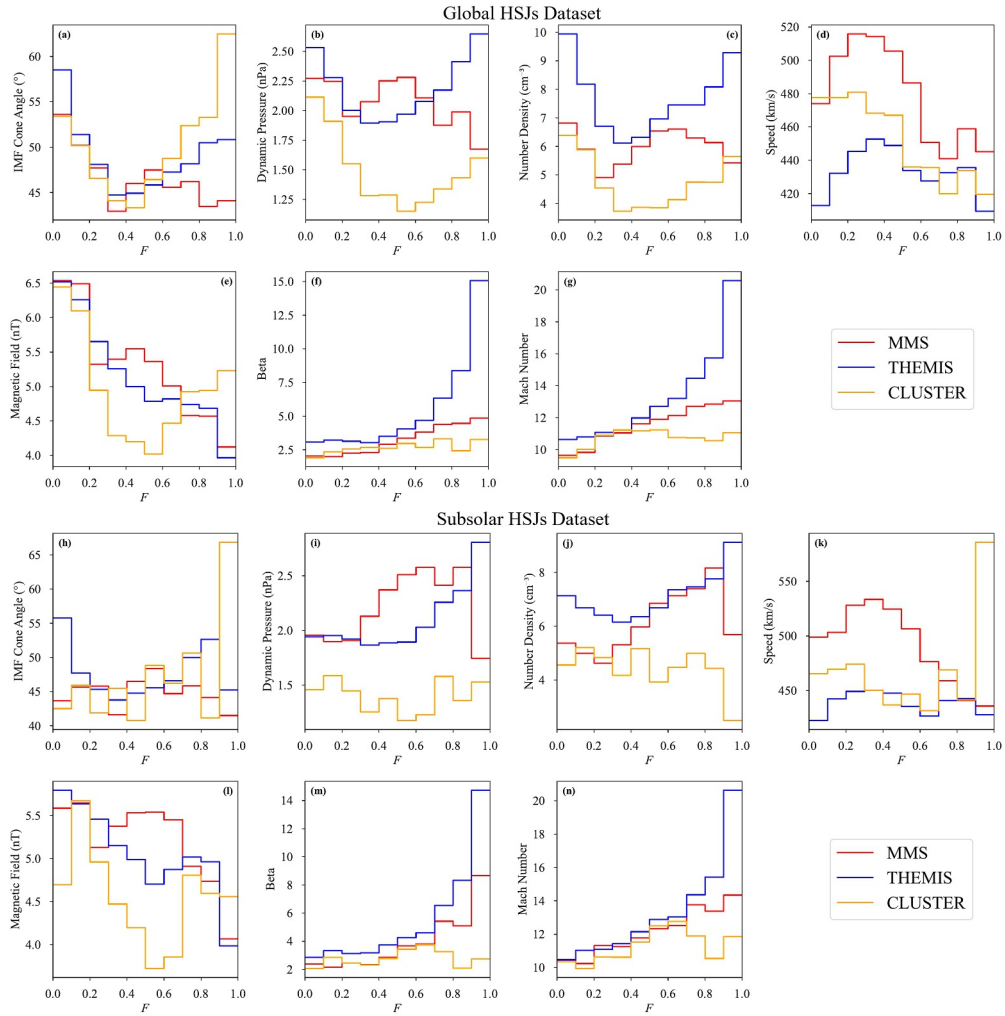

Figure 5. Mean solar wind conditions for global and subsolar high-speed jet (HSJ) data sets from MMS, THEMIS, and Cluster missions, Binned by Fractional Magnetosheath Distance. (a–g) Mean solar wind conditions for global HSJs data set. (h–n) Mean solar wind conditions for subsolar HSJs data set. Solar wind parameters include: (a/h) IMF cone angle, (b/i) dynamic pressure, (c/j) ion density, (d/k) solar wind speed, (e/l) IMF $|B|$, (f/m) plasma beta, and (g/n) Alfvén Mach number. Red, blue, and yellow lines represent the mean solar wind conditions derived from MMS, THEMIS, and Cluster data, respectively. The selection of solar wind parameters refers to the literature by Vuorinen, Hietala, et al. (2023).

magnetopause ($F \sim 0.4$), the V_x of HSJs begins to decrease at a faster rate than that of the background flow (Figure 6a). This phenomenon can be explained by the deflection of HSJs near the magnetopause, by which a part of V_x component has been diverted into V_y and V_z components (or transverse component) as shown in Figure 6b. Near the bow shock ($F > 0.9$), where the HSJs are initially formed, the V_x component is slightly dominant over the transverse component, indicating that the HSJs propagation direction tends to be in the Sun-Earth direction, while near the magnetopause their transverse speed becomes dominant. When the HSJs propagate in the magnetosheath, the transverse velocity remains nearly constant before approaching the magnetopause (Figure 6b). After they penetrate deep into the magnetosheath ($F < 0.4$), their transverse velocity starts to increase and becomes much larger than the V_x component (Figure 6b), showing a significant deviation from the Sun-Earth line. Given that the background magnetosheath flow exhibits only weak acceleration, the enhancement of the transverse velocity must be attributed to the deflection of HSJs, rather than the background flow. As illustrated in Figures 6c and 6d, HSJ dynamic pressure decreases continuously from the bow shock to the magnetopause, while HSJ density first increases and then gradually decreases—mirroring the trend of the ambient magnetosheath. Consequently, the reduction in HSJ dynamic pressure is primarily attributed to decreasing velocity. As HSJs propagate deeper into the magnetosheath, the differences in ion density and dynamic pressure between the jets and the surrounding sheath gradually diminish, which aligns with the findings of Palmroth et al. (2021).

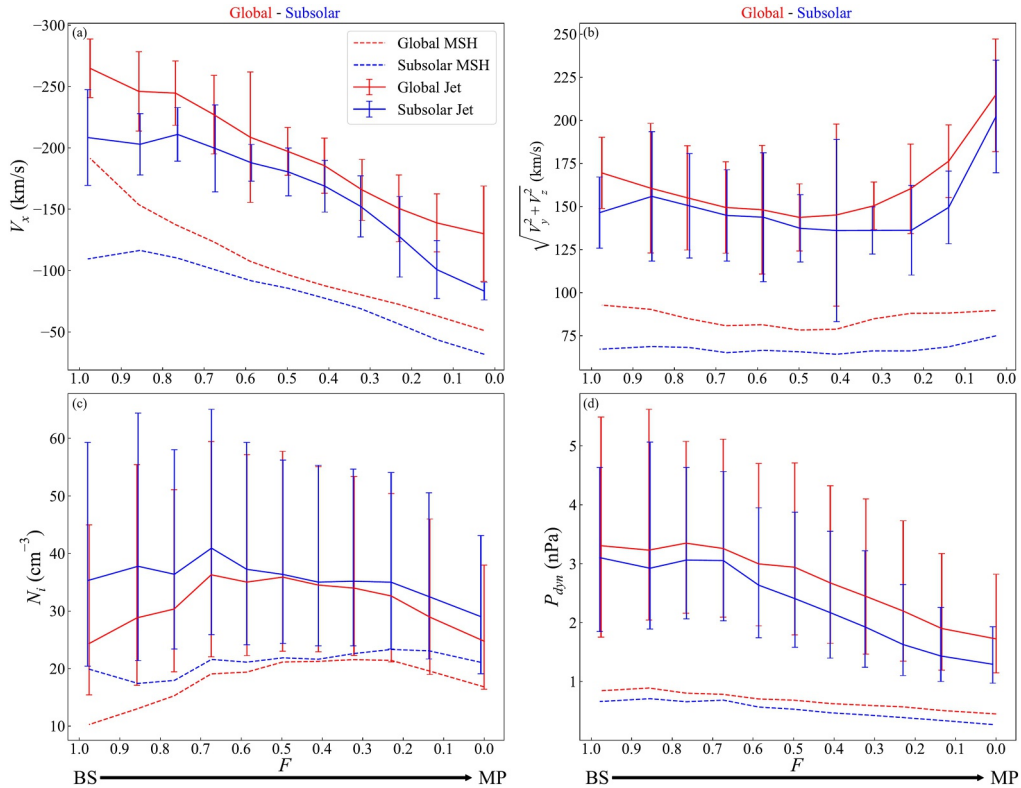

Figure 6. Overview of high-speed jets (HSJs) evolution. (a) Median x-component(GSE) velocity of HSJs in different fractional magnetosheath distance $[F]$, (b) Median yz-components(GSE) velocity of HSJs in different F, (c) Median ion density of HSJs in different F, (d) Median dynamic pressure of HSJs in different F. The red and blue lines represent results for the global and subsolar magnetosheath regions, respectively, with error bars corresponding to the first and third quartiles. Additionally, solid lines denote jet velocities, while dashed lines indicate magnetosheath background velocities—both of which are median values.

In Figure 7, we further compare the velocity evolution presented in Figures 6a and 6b with those obtained from the 3D global hybrid simulation under a radial interplanetary magnetic field (Ren, Guo, et al., 2024). To enhance comparability with observational results (red line in Figures 6a and 6b), the blue line in Figure 7 denotes simulation outcomes restricted to the magnetosheath region within the z-axis range of $[-5, 5]R_E$. The velocity

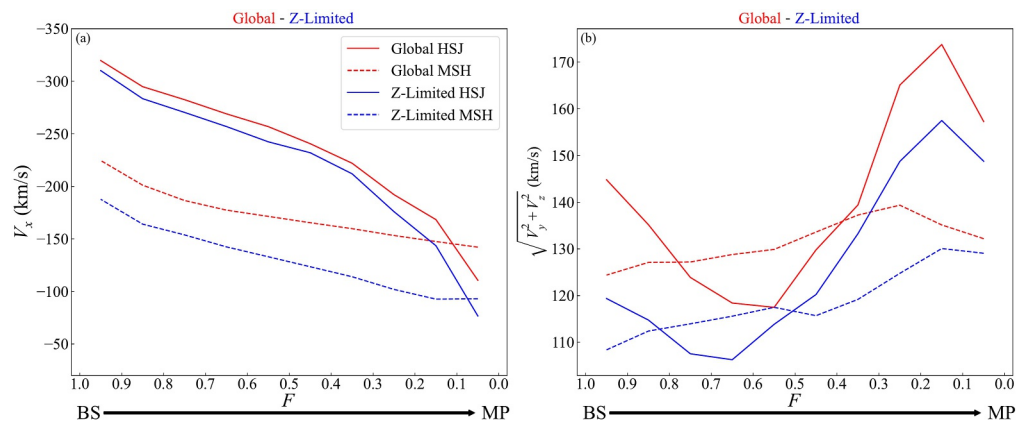

Figure 7. Velocity Evolution of high-speed jets (HSJs) in 3D Simulation. (a) Median x-component (GSE) velocity of HSJs at different fractional magnetosheath distances $[F]$, (b) Median yz-component (GSE) velocity of HSJs at different F. Red and blue lines denote results for the global magnetosheath and the magnetosheath region limited to z-axis $[-5, 5]R_E$, respectively. Solid and dashed lines represent HSJ velocity and magnetosheath background velocity, respectively.

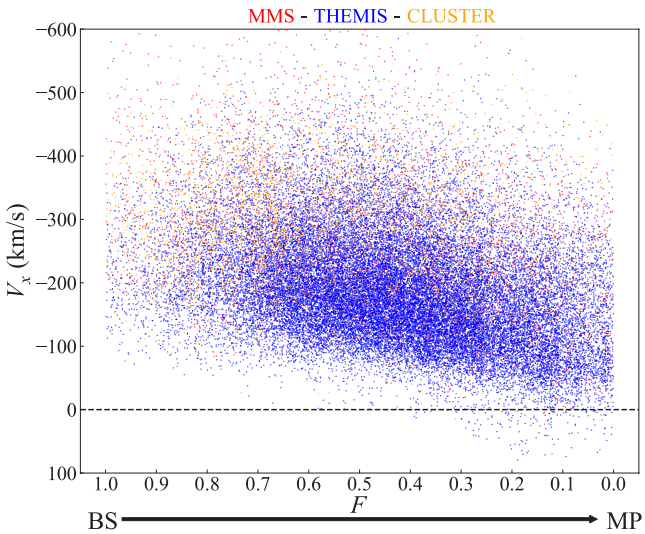

Figure 8. The scatter plot showcases global HSJs' $V_{x,\mathrm{GSE}}$ from various satellite missions. The black dashed line denotes $V_{x,\mathrm{GSE}} = 0$, with data points below it indicating sunward flow ($V_{x,\mathrm{GSE}} < 0$).

evolution patterns between the observations and simulations are essentially consistent: specifically, from the bow shock to the magnetopause, the x-component of velocity V_x decreases, while the $V_{y,z}$ increase.

For a more detailed understanding of the evolution of HSJs, we present a scatter plot of all HSJs in the (V_x, F) plane in Figure 8. Each dot represents a HSJ. The V_x component of HSJs has a broad range from −600 to 100 km/s, with a notable concentration within the range of −300 to −50 km/s. Consistent with the trend shown in Figure 6a, there is also a clear declining trend for the anti-sunward speed as the HSJs propagate toward the magnetopause. More importantly, we find that in the vicinity of the magnetopause, some HSJs even have the sunward velocities. This can be explained by the "Indentation-Rebounce-Relaxation" sequence established by Ma et al. (2024), which describes the magnetopause's response to the impact of the HSJ. During the "Rebounce" phase, the indentation of the magnetopause tends to recover, which in turn drives the HSJ to move in the sunward direction.

To further investigate the propagation direction of HSJs in the (y, z) plane, we have divided the dayside magnetosheath into four quadrants as shown in Figure 9. In each quadrant, the velocity vector in the (y, z) plane will be established by calculating the median value of V_y and V_z in each F bin. Figure 10 illustrates four slices at various distances from the bow shock to the magnetopause. Near the bow shock ($F = 0.86$), the HSJs are generated with a propagation direction distribution that is nearly isotropic in the (y, z) plane. The isotropic distribution of the transverse velocities remains nearly unchanged during the propagation of HSJs, even when they reach the magnetopause. HSJ velocities closely follow the direction of the background magnetosheath plasma (dashed line) but are larger in magnitude. Notably, velocity magnitudes are slightly lower in Quadrants 2 and 3 than in 1 and 4, revealing a subtle dawn-dusk asymmetry—one that is also observed in the background flow. This consistency is anticipated: magnetosheath speed is favored duskward (Dimmock et al., 2017). Even at an IMF cone angle of 30°, the asymmetry remains clear, likely driven by velocity deviations at the bow shock that depend on the IMF-shock normal angle (Turc et al., 2020). Collectively, this may indicate that HSJ velocity directions are governed by magnetosheath flows early on and throughout the entire evolution process.

The simulation results are displayed in Figure 11 in the same format as Figure 10. Overall, the simulation results also demonstrate the isotropic distribution of the propagation direction of HSJs in the (y, z) plane from the bow shock to magnetopause. The 3D simulation yielded consistent results with Suni et al. (2025): the transverse speed of HSJs, even at their formation, aligns with the background flow in the $\pm Vy$ direction. However, compared with the observations, the simulation results exhibit a higher degree of isotropy, with the velocity directions in the four quadrants tending to align more closely with the dotted gray line (45/135°) in GSE coordinates (Figure 11). This outcome is reasonable considering that the simulation encompasses the high-latitude region in the magnetosheath, an area that is scarcely covered by observations due to the limited inclination of MMS and THEMIS satellites. When we limited the simulation z-axis to the range of [−5, 5] R_E, then the discrepancy of bulk velocity directions for simulation and observations becomes smaller (not shown), confirming that it is due to limited high-latitude coverage. Removing solar wind orbital aberration (about 30 km/s) from Earth's orbital motion weakens the dawn-dusk anisotropy (which persists), making results more consistent with simulations (See the Supporting Information S1). The good consistency between the simulation results (Figure 11) and observations (Figure 10) indicates that the transverse velocity of HSJs $V_{y,z}$ tends to align with the ambient magnetosheath flow early on.

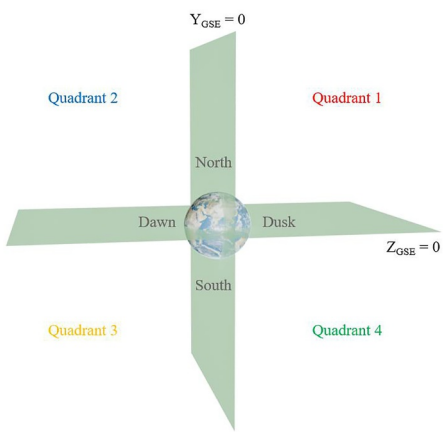

Figure 9. Sketch of four quadrants of the Earth. In the yz plane of the GSE coordinates, the Earth can be divided into 4 quadrants. Quadrants 1 to 4 are illustrated in red, blue, orange and green colors, respectively.

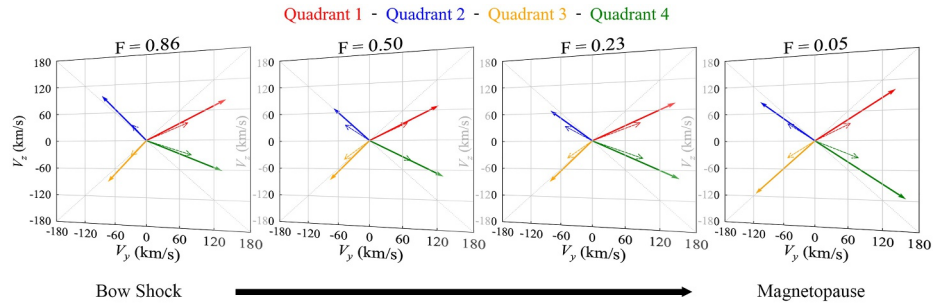

Figure 10. Evolution of the median *yz*-components (GSE) velocity vectors of global High-speed jets. We only present four representative Figures depicting various stages of the evolution process here, with corresponding fractional magnetosheath distance (F) of 0.86, 0.50, 0.23 and 0.05, respectively. The velocity vectors in red, blue, yellow, and green represent the four quadrants as illustrated in Figure 9. Solid lines represent the median velocity vectors of global HSJs, whereas dashed lines denote the median background flow of the magnetosheath.

4. Conclusions and Discussion

A comprehensive understanding of HSJ evolution during magnetosheath penetration is fundamental for modeling and predicting their impact on the magnetopause. In this study, by combining multi-satellite data from MMS (2015–2023), THEMIS (2008–2023), and Cluster (2001–2020), we have compiled a comprehensive data set of nearly 40,000 HSJs to statistically study the velocity evolution of HSJs from the bow shock to the magnetopause for the first time. We find that the occurrence rate of HSJs depends on their relative position F in the magnetosheath, reaching its peak with $F \approx 0.6$, that is, around the middle region. On average, HSJs can be observed approximately 2.85 times per hour in the subsolar dayside magnetosheath. Moreover, the V_x component of HSJs continues to decrease until they reach the magnetopause, where HSJs are deflected and their V_y and V_z components are suddenly enhanced. Interestingly, some HSJs are observed to propagate sunward near the magnetopause, which may be due to the magnetopause rebounding following the impact of HSJs. 3D global hybrid simulations under radial IMF successfully replicate both the isotropic distribution of the HSJ velocity in the transverse plane and the alignment of their velocity with the background flow. This good agreement between observations and simulations suggests that HSJ transverse velocity aligns with the ambient magnetosheath flow from an early stage.

In this study, we selected HSJs based on local plasma parameters, when the peak dynamic pressure exceeded 2.5-fold 20-min mean background flow. This threshold is lower than in previous studies (Koller et al., 2022), which used a threefold increase, to specifically include relatively weaker HSJs close to the magnetopause in our data set. Therefore, when moving towards the magnetopause, there is likely a bias towards originally stronger jets that still fulfill the jet criterion close to the magnetopause. While the stricter HSJ criterion used here may reduce the bias, it still exists. Assuming HSJs form exclusively at the shock, a stricter criterion would result in more of the weaker

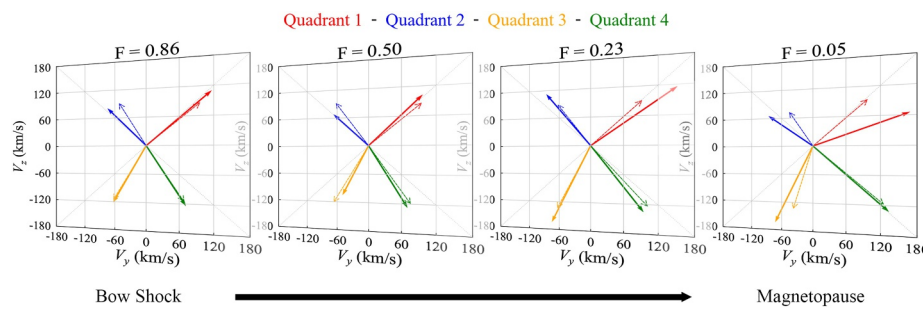

Figure 11. Simulation results illustrating the evolution of the median velocity vectors of global High-speed jets (HSJs) in the *yz*-plane of GSE coordinates under a radial interplanetary magnetic field. For a detailed description of the simulation model, please refer to Ren, Guo, et al. (2024). To compare with the statistical results, we provide four representative Figures with corresponding fractional magnetosheath distances similar to those in Figure 10. The velocity vectors in red, blue, yellow, and green represent the four quadrants as illustrated in Figure 9. Solid lines represent the median velocity vectors of global HSJs, whereas dashed lines denote the median background flow of the magnetosheath.

HSJs being observed near the shock, whereas their counterparts near the magnetopause would again fall below the threshold.

Tinoco-Arenas et al. (2022) used local 2D hybrid simulations and found that, across all observation-based criteria, the number of jets decreases with distance from the shock. In contrast, Poeppelwerth et al. (2024) reported that, for the three most-widely used jet criteria (M. O. Archer & Horbury, 2013; Koller et al., 2022; Plaschke et al., 2013), jet occurrence is more concentrated in the middle of the magnetosheath (Krämer et al., 2025). Our results align with those of Poeppelwerth et al. (2024) and differ from Tinoco-Arenas et al. (2022), likely due to the limitations of the local 2D simulation configuration.

Different spacecraft missions observe varying occurrence rates of jets, with the primary cause of this discrepancy being that each mission operated under distinct solar wind conditions. This observation implies that integrating data sets from multiple missions offers a viable approach to align the combined observational context more closely with the true distribution of solar wind parameters, thereby reducing biases associated with mission-specific solar wind variability.

Consistent with Goncharov (Goncharov et al., 2020) and Echim (Echim et al., 2023), the transverse velocity of HSJs tends to align with the ambient magnetosheath flow. Furthermore, this alignment persists from the vicinity of the bow shock to the magnetopause—suggesting either that the background magnetosheath flow influences the HSJ propagation direction early on, or that their formation mechanism(s) favor the creation of structures propagating transversely in the same direction as the background magnetosheath plasma. Additionally, the magnitude of HSJ velocity exhibits a slight dusk-favored asymmetry, as for the bulk magnetosheath flow.

Raptis et al. (2020) presented histograms of the V_x, V_y, and V_z components for distinct jet categories and also documented the presence of HSJs with positive V_x (sunward velocity). We replicated this analysis using our MMS data set (results not shown), and the derived velocity distributions align closely with the average of the blue (quasi-parallel HSJ) and red (quasi-perpendicular HSJ) curves in Figure 9 of Raptis et al. (2020). We further investigated the transverse flow pattern $V_{y,z}$ of HSJs with IMF cone angle more than 30° (not shown), and it exhibits no significant differences from Figure 10. This observation, however, is based on a limited sample size. To derive more robust statistical results, expanding the data set to include more high-latitude HSJ events is therefore necessary, and further studies are required in this regard.

By analyzing several HSJs detected by MMS satellites, Ma et al. (2024) revealed the response pattern of the magnetopause to the HSJ impact, which is described as the "Indentation-Rebounce-Relaxation" sequence. In this sequence, during the rebounce of the magnetopause, the HSJ can be redirected backwards, resulting in the positive V_x near the magnetopause. As shown in Figure 6, it is clearly found that there are a fraction of HSJs propagating sunward close to the magnetopause, supporting the "Indentation-Rebounce-Relaxation" sequence. Guo et al. (2022) discovered that the elongated HSJs formed at the quasi-parallel shock extend toward the quasi-perpendicular magnetosheath along with the background magnetosheath flow, which may support the HSJ velocity distribution in the *yz*-plane; while Ren, Guo, et al. (2024) further demonstrated a honeycomb-like magnetosheath forms potentially due to the evenly distributed bulk velocities of a cluster of HSJs in the *yz*-plane. Therefore, our study may offer novel perspectives for a more profound understanding of the generation and evolution of HSJs.

Conflict of Interest

The authors declare no conflicts of interest relevant to this study.

Data Availability Statement

We provide the global magnetosheath jet lists (local criteria for MMS, THEMIS and Cluster) at https://osf.io/gaueq (Y. Wang, 2025). The data of each mission (MMS, THEMIS, and Cluster) were sourced from the Space Physics Data Facility (SPDF) website https://spdf.gsfc.nasa.gov/pub/data/. The OMNI solar wind data were obtained from http://spdf.gsfc.nasa.gov/pub/data/omni/. The simulation data were obtained from Ren and Guo (2024).

Acknowledgments
This research was funded by the NSFC Grants 42322406 and 42230201 the "USTC Tang Scholar" program, and the Fundamental Research Funds for the Central Universities (KY2080000063 and KY2080000138). We gratefully acknowledge MMS team, THEMIS team and Cluster team for providing data and support (https://spdf.gsfc.nasa.gov/pub/data/). Furthermore, we acknowledge use of NASA/GSFC's Space Physics Data Facility's OMNIWeb service, and OMNIdata.

References

Angelopoulos, V. (2008). The themis mission. *Space Science Reviews*, *141*(1–4), 5–34. [Review]. https://doi.org/10.1007/s11214-008-9336-1

Archer, M., Hietala, H., Hartinger, M., Plaschke, F., & Angelopoulos, V. (2019). Direct observations of a surface eigenmode of the dayside magnetopause. *Nature Communications*, *10*(1), 615. [Article]. https://doi.org/10.1038/s41467-018-08134-5

Archer, M. O., & Horbury, T. S. (2013). Magnetosheath dynamic pressure enhancements: Occurrence and typical properties. *Annales Geophysicae*, *31*(2), 319–331. https://doi.org/10.5194/angeo-31-319-2013

Archer, M. O., Horbury, T. S., & Eastwood, J. P. (2012). Magnetosheath pressure pulses: Generation downstream of the bow shock from solar wind discontinuities. *Journal of Geophysical Research*, *117*(A5). [Article]. https://doi.org/10.1029/2011JA017468

Auster, H. U., Glassmeier, K. H., Magnes, W., Aydogar, O., Baumjohann, W., Constantinescu, D., et al. (2008). The themis fluxgate magnetometer. *Space Science Reviews*, *141*(1–4), 235–264. [Review]. https://doi.org/10.1007/s11214-008-9365-9

Balogh, A., Dunlop, M., Cowley, S., Southwood, D., Thomlinson, J., Glassmeier, K., et al. (1997). The cluster magnetic field investigation. *Space Science Reviews*, *79*(1–2), 65–91. [Article]. https://doi.org/10.1023/A:1004970907748

Burch, J. L., Moore, T. E., Torbert, R. B., & Giles, B. L. (2016). Magnetospheric multiscale overview and science objectives. *Space Science Reviews*, *199*(1–4), 5–21. [Review]. https://doi.org/10.1007/s11214-015-0164-9

Chao, J., Wu, D., Lin, C.-H., Yang, Y.-H., Wang, X., Kessel, M., et al. (2002). Models for the size and shape of the earth's magnetopause and bow shock. *COSPAR Colloquia Series*. https://doi.org/10.1016/S0964-2749(02)80212-8

Dandouras, I., Barthe, A., Penou, E., Brunato, S., Rème, H., Kistler, L., et al. (2010). Cluster ion spectrometry (cis) data in the cluster active archive (caa). In *The cluster active archive: Studying the earth's space plasma environment* (pp. 51–72).

Dimmock, A. P., Nykyri, K., Osmane, A., Karimabadi, H., & Pulkkinen, T. I. (2017). Dawn-dusk asymmetries of the earth's dayside magnetosheath in the magnetosheath interplanetary medium reference frame. In *Dawn-dusk asymmetries in planetary plasma environments* (pp. 49–72). American Geophysical Union (AGU). https://doi.org/10.1002/9781119216346.ch5

Dmitriev, A. V., & Suvorova, A. V. (2012). Traveling magnetopause distortion related to a large-scale magnetosheath plasma jet: Themis and ground-based observations. *Journal of Geophysical Research*, *117*(A8). [Article]. https://doi.org/10.1029/2011JA016861

Dmitriev, & Suvorova. (2015). Large-scale jets in the magnetosheath and plasma penetration across the magnetopause: Themis observations. *Journal of Geophysical Research: Space Physics*. [Article]. https://doi.org/10.1002/2014JA020953

Echim, M., Voiculescu, M., Munteanu, C., Teodorescu, E., Voitcu, G., Negrea, C., et al. (2023). On the phenomenology of magnetosheath jets with insight from theory, modelling, numerical simulations and observations by cluster spacecraft. *Frontiers in Astronomy and Space Sciences, Volume10-2023*, *10*, 1094282. https://doi.org/10.3389/fspas.2023.1094282

Escoubet, C., Fehringer, M., & Goldstein, M. (2001). The cluster mission - Introduction [Editorial Material]. *Annales Geophysicae*, *19*(10–12, SI), 1197–1200. https://doi.org/10.5194/angeo-19-1197-2001

Fatemi, S., Hamrin, M., Kramer, E., Gunell, H., Nordin, G., Karlsson, T., & Goncharov, O. (2024). Unveiling the 3d structure of magnetosheath jets. *Monthly Notices of the Royal Astronomical Society*, *531*(4), 4692–4713. [Article]. https://doi.org/10.1093/mnras/stae1456

Goncharov, O., Gunell, H., Hamrin, M., & Chong, S. (2020). Evolution of high-speed jets and plasmoids downstream of the quasi-perpendicular bow shock. *Journal of Geophysical Research: Space Physics*, *125*(6), e2019JA027667. https://doi.org/10.1029/2019JA027667

Guo, J., Lu, S., Lu, Q., Lin, Y., Wang, X., Ren, J., et al. (2022). Large-scale high-speed jets in earth's magnetosheath: Global hybrid simulations. *Journal of Geophysical Research: Space Physics*, *127*(6), e2022JA030477. [Article]. https://doi.org/10.1029/2022JA030477

Han, D.-S., Hietala, H., Chen, X.-C., Nishimura, Y., Lyons, L. R., Liu, J.-J., et al. (2017). Observational properties of dayside throat aurora and implications on the possible generation mechanisms. *Journal of Geophysical Research: Space Physics*, *122*(2), 1853–1870. https://doi.org/10.1002/2016JA023394

Hietala, H., Laitinen, T. V., Andréeová, K., Vainio, R., Vaivads, A., Palmroth, M., et al. (2009). Supermagnetosonic jets behind a collisionless quasiparallel shock. *Physical Review Letters*, *103*(24), 245001. https://doi.org/10.1103/physrevlett.103.245001

Hietala, H., Phan, T. D., Angelopoulos, V., Oieroset, M., Archer, M. O., Karlsson, T., & Plaschke, F. (2018). In situ observations of a magnetosheath high-speed jet triggering magnetopause reconnection. *Geophysical Research Letters*, *45*(4), 1732–1740. https://doi.org/10.1002/2017GL076525

Hietala, H., & Plaschke, F. (2013). On the generation of magnetosheath high-speed jets by bow shock ripples. *Journal of Geophysical Research: Space Physics*, *118*(11), 7237–7245. [Article]. https://doi.org/10.1002/2013JA019172

Karimabadi, H., Roytershteyn, V., Vu, H., Omelchenko, Y., Scudder, J., Daughton, W., et al. (2014). The link between shocks, turbulence, and magnetic reconnection in collisionless plasmas. *Physics of Plasmas*, *21*(6), 062308. [Article]. https://doi.org/10.1063/1.4882875

Karlsson, T., Kullen, A., Liljeblad, E., Brenning, N., Nilsson, H., Gunell, H., & Hamrin, M. (2015). On the origin of magnetosheath plasmoids and their relation to magnetosheath jets. *Journal of Geophysical Research: Space Physics*, *120*(9), 7390–7403. [Article]. https://doi.org/10.1002/2015JA021487

Koller, F., Temmer, M., Preisser, L., Plaschke, F., Geyer, P., Jian, L. K., et al. (2022). Magnetosheath jet occurrence rate in relation to cmes and sirs. *Journal of Geophysical Research: Space Physics*, *127*(4), e2021JA030124. https://doi.org/10.1029/2021JA030124

Krämer, E., Koller, F., Suni, J., LaMoury, A. T., Pöppelwerth, A., Glebe, G., et al. (2025). Jets downstream of collisionless shocks: Recent discoveries and challenges. *Space Science Reviews*, *221*(1), 4. [Article]. https://doi.org/10.1007/s11214-024-01129-3

LaMoury, A. T., Hietala, H., Plaschke, F., Vuorinen, L., & Eastwood, J. P. (2021). Solar wind control of magnetosheath jet formation and propagation to the magnetopause. *Journal of Geophysical Research: Space Physics*, *126*(9), e2021JA029592. [Article]. https://doi.org/10.1029/2021JA029592

Liu, T. Z., Hietala, H., Angelopoulos, V., Omelchenko, Y., Vainio, R., & Plaschke, F. (2020). Statistical study of magnetosheath jet-driven bow waves. *Journal of Geophysical Research: Space Physics*, *125*(7), e2019JA027710. [Article]. https://doi.org/10.1029/2019JA027710

Ma, J., Tang, B., Gao, X., Li, W., Lu, Q., Guo, W., et al. (2024). The comprehensive response of the magnetopause to the impact of an isolated magnetosheath high-speed jet. *Geophysical Research Letters*, *51*(21), e2024GL111132. [Article]. https://doi.org/10.1029/2024GL111132

McFadden, J. P., Carlson, C. W., Larson, D., Ludlam, M., Abiad, R., Elliott, B., et al. (2008). The themis esa plasma instrument and in-flight calibration. *Space Science Reviews*, *141*(1–4), 277–302. [Review]. https://doi.org/10.1007/s11214-008-9440-2

Nemecek, Z., Safrankova, J., Prech, L., Sibeck, D., Kokubun, S., & Mukai, T. (1998). Transient flux enhancements in the magnetosheath. *Geophysical Research Letters*, *25*(8), 1273–1276. [Article]. https://doi.org/10.1029/98GL50873

Osmane, A., & Raptis, S. (2024). On the formation of super-alfvénic flows downstream of collisionless shocks. *The Astrophysical Journal*, *976*(1), 104. https://doi.org/10.3847/1538-4357/ad8570

Palmroth, M., Raptis, S., Suni, J., Karlsson, T., Turc, L., Johlander, A., et al. (2021). Magnetosheath jet evolution as a function of lifetime: Global hybrid-vlasov simulations compared to mms observations. *Annales Geophysicae*, *39*(2), 289–308. https://doi.org/10.5194/angeo-39-289-2021

Plaschke, F., Hietala, H., & Angelopoulos, V. (2013). Anti-sunward high-speed jets in the subsolar magnetosheath. *Annales Geophysicae*, *31*(10), 1877–1889. https://doi.org/10.5194/angeo-31-1877-2013

Plaschke, F., Hietala, H., Archer, M., Blanco-Cano, X., Kajdic, P., Karlsson, T., et al. (2018). Jets downstream of collisionless shocks. *Space Science Reviews*, *214*(5), 81. [Review]. https://doi.org/10.1007/s11214-018-0516-3

Plaschke, F., Karlsson, T., Hietala, H., Archer, M., Vörös, Z., Nakamura, R., et al. (2017). Magnetosheath high-speed jets: Internal structure and interaction with ambient plasma. *Journal of Geophysical Research: Space Physics*, *122*(10). [Article]. https://doi.org/10.1002/2017JA024471

Poeppelwerth, A., Koller, F., Grimmich, N., Constantinescu, D., Glebe, G., Voeroes, Z., & Plaschke, F. (2024). Cluster: List of plasma jets in the subsolar magnetosheath. *Frontiers in Astronomy and Space Sciences*, *11*. [Article]. https://doi.org/10.3389/fspas.2024.1388307

Pollock, C., Moore, T., Jacques, A., Burch, J., Gliese, U., Saito, Y., et al. (2016). Fast plasma investigation for magnetospheric multiscale. *Space Science Reviews*, *199*(1–4), 331–406. [Review]. https://doi.org/10.1007/s11214-016-0245-4

Preisser, L., Blanco-Cano, X., Kajdič, P., Burgess, D., & Trotta, D. (2020). Magnetosheath jets and plasmoids: Characteristics and formation mechanisms from hybrid simulations. *The Astrophysical Journal Letters*, *900*(1), L6. [Article]. https://doi.org/10.3847/2041-8213/abad2b

Raptis, S., Karlsson, T., Plaschke, F., Kullen, A., & Lindqvist, P.-A. (2020). Classifying magnetosheath jets using mms: Statistical properties. *Journal of Geophysical Research: Space Physics*, *125*(11), e2019JA027754. [Article]. https://doi.org/10.1029/2019JA027754

Raptis, S., Karlsson, T., Vaivads, A., Lindberg, M., Johlander, A., & Trollvik, H. (2022a). On magnetosheath jet kinetic structure and plasma properties. *Geophysical Research Letters*, *49*(21), e2022GL100678. [Article]. https://doi.org/10.1029/2022GL100678

Raptis, S., Karlsson, T., Vaivads, A., Pollock, C., Plaschke, F., Johlander, A., et al. (2022b). Downstream high-speed plasma jet generation as a direct consequence of shock reformation. *Nature Communications*, *13*(1), 598. [Article]. https://doi.org/10.1038/s41467-022-28110-4

Rème, H., Aoustin, C., Bosqued, M., Dandouras, I., Lavraud, B., Sauvaud, J., & Sonnerup, B. (2001). First multispacecraft ion measurements in and near the earth's magnetosphere with the identical cluster ion spectrometry (cis) experiment. *Annales Geophysicae*, *19*(10–12, SI), 1303–1354. [Article]. https://doi.org/10.5194/angeo-19-1303-2001

Ren, J., & Guo, J. (2024). Data for "The formation of honeycomb-like magnetosheath jets: Three-dimensional global hybrid simulations"[DS/OL] [Dataset]. *Science Data Bank*. https://doi.org/10.57760/sciencedb.18059

Ren, J., Guo, J., Lu, Q., Lu, S., Gao, X., Ma, J., & Wang, R. (2024a). Honeycomb-like magnetosheath structure formed by jets: Three-dimensional global hybrid simulations. *Geophysical Research Letters*, *51*(12), e2024GL109925. [Article]. https://doi.org/10.1029/2024GL109925

Ren, J., Lu, Q., Gao, X., Gedalin, M., Qiu, H., Han, D., & Wang, R. (2024b). Hybrid simulation of magnetosheath jet-driven bow waves. *Geophysical Research Letters*, *51*(5), e2023GL106606. [Article]. https://doi.org/10.1029/2023GL106606

Ren, J., Lu, Q., Guo, J., Gao, X., Lu, S., Wang, S., & Wang, R. (2023). Two-dimensional hybrid simulations of high-speed jets downstream of quasi-parallel shocks. *Journal of Geophysical Research: Space Physics*, *128*(8), e2023JA031699. [Article]. https://doi.org/10.1029/2023JA031699

Russell, C. T., Anderson, B. J., Baumjohann, W., Bromund, K. R., Dearborn, D., Fischer, D., et al. (2016). The magnetospheric multiscale magnetometers. *Space Science Reviews*, *199*(1–4), 189–256. [Review]. https://doi.org/10.1007/s11214-014-0057-3

Shue, J., Song, P., Russell, C., Steinberg, J., Chao, J., Zastenker, G., et al. (1998). Magnetopause location under extreme solar wind conditions. *Journal of Geophysical Research*, *103*(A8), 17691–17700. [Article]. https://doi.org/10.1029/98JA01103

Shue, J. H., Chao, J. K., Song, P., McFadden, J. P., Suvorova, A., Angelopoulos, V., et al. (2009). Anomalous magnetosheath flows and distorted subsolar magnetopause for radial interplanetary magnetic fields. *Geophysical Research Letters*, *36*(18). [Article]. https://doi.org/10.1029/2009GL039842

Song, X., Pingbing, Z., & Zilu, Z. (2021). Automatic identification of magnetopause crossing events. *Chinese Journal of Space Science*, *41*(3), 375–383. https://doi.org/10.11728/cjss2021.03.375

Suni, J., Palmroth, M., Turc, L., Battarbee, M., Johlander, A., Tarvus, V., et al. (2021). Connection between foreshock structures and the generation of magnetosheath jets: Vlasiator results. *Geophysical Research Letters*, *48*(20), e2021GL095655. https://doi.org/10.1029/2021GL095655

Suni, J., Palmroth, M., Turc, L., Battarbee, M., Pfau-Kempf, Y., & Ganse, U. (2025). Magnetosheath jets associated with a solar wind rotational discontinuity in a hybrid-vlasov simulation. *Journal of Geophysical Research: Space Physics*, *130*(6), e2025JA033995. https://doi.org/10.1029/2025JA033995

Tinoco-Arenas, A., Kajdič, P., Preisser, L., Blanco-Cano, X., Trotta, D., & Burgess, D. (2022). Parametric study of magnetosheath jets in 2d local hybrid simulations. *Frontiers in Astronomy and Space Sciences*, *9*, 793195. https://doi.org/10.3389/fspas.2022.793195

Turc, L., Tarvus, V., Dimmock, A. P., Battarbee, M., Ganse, U., Johlander, A., et al. (2020). Asymmetries in the earth's dayside magnetosheath: Results from global hybrid-vlasov simulations. *Annales Geophysicae*, *38*(5), 1045–1062. https://doi.org/10.5194/angeo-38-1045-2020

Vuorinen, L., Hietala, H., Lamoury, A. T., & Plaschke, F. (2023a). Solar wind parameters influencing magnetosheath jet formation: Low and high imf cone angle regimes. *Journal of Geophysical Research: Space Physics*, *128*(10), e2023JA031494. [Article]. https://doi.org/10.1029/2023JA031494

Vuorinen, L., LaMoury, A. T., Hietala, H., & Koller, F. (2023b). Magnetosheath jets over solar cycle 24: An empirical model. *Journal of Geophysical Research: Space Physics*, *128*(8), e2023JA031493. https://doi.org/10.1029/2023JA031493

Vuorinen, L., Vainio, R., Hietala, H., & Liu, T. Z. (2022). Monte carlo simulations of electron acceleration at bow waves driven by fast jets in the earth's magnetosheath. *The Astrophysical Journal*, *934*(2), 165. [Article]. https://doi.org/10.3847/1538-4357/ac7f42

Wang, B., Nishimura, Y., Hietala, H., Lyons, L., Angelopoulos, V., Plaschke, F., et al. (2018). Impacts of magnetosheath high-speed jets on the magnetosphere and ionosphere measured by optical imaging and satellite observations. *Journal of Geophysical Research: Space Physics*, *123*(6), 4879–4894. https://doi.org/10.1029/2017JA024954

Wang, Y. (2025). Multi-mission hsjs dataset (mms, themis, cluster) [Dataset]. *Open Science Framework*. https://doi.org/10.17605/OSF.IO/ZDUFK

Wang, Z., Han, D., Chen, X., Shi, R., Teng, S., Zhang, J., et al. (2025). Observations of a throat aurora directly driven by magnetosheath high-speed jet. *Journal of Geophysical Research: Space Physics*, *130*(1), e2024JA033276. [Article]. https://doi.org/10.1029/2024JA033276

Zhou, X., Gao, X., Lu, Q., Hajra, R., Ke, Y., Chen, R., & Ma, J. (2024). Prompt disappearance of magnetospheric chorus waves caused by high-speed magnetosheath jets. *Journal of Geophysical Research: Space Physics*, *129*(6), e2024JA032576. [Article]. https://doi.org/10.1029/2024JA032576

Zhou, Y., Shen, C., & Ji, Y. (2023). Undulated shock surface formed after a shock–discontinuity interaction. *Geophysical Research Letters*, *50*(10), e2023GL103848. [Article]. https://doi.org/10.1029/2023GL103848